RESEARCH ARTICLE

WILEY

Fast interfacial electrocatalytic desolvation enabling low-temperature and long-cycle-life aqueous Zn batteries

Jian Wang[1,2,3] | Hongfei Hu[1] | Lujie Jia[1] | Jing Zhang[1] | Quan Zhuang[4] | Linge Li[1] | Yongzheng Zhang[5] | Dong Wang[6] | Qinghua Guan[1] | Huimin Hu[1] | Meinan Liu[1] | Liang Zhan[5] | Henry Adenusi[7,8,9] | Stefano Passerini[2,3,10] | Hongzhen Lin[1]

[1]i-Lab & CAS Key Laboratory of Nanophotonic Materials and Devices, Suzhou Institute of Nano-Tech and Nano-Bionics, Chinese Academy of Sciences, Suzhou, China

[2]Helmholtz Institute Ulm (HIU), Ulm, Germany

[3]Karlsruhe Institute of Technology (KIT), Karlsruhe, Germany

[4]Inner Mongolia Key Laboratory of Carbon Nanomaterials, Nano Innovation Institute (NII), Inner Mongolia Minzu University, Tongliao, China

[5]State Key Laboratory of Chemical Engineering, East China University of Science and Technology, Shanghai, China

[6]School of Materials Science & Engineering and International Center of Future Science, Jilin University, Changchun, Jilin, China

[7]Department of Science and Engineering of Matter, Environment and Urban Planning, Marche Polytechnic University, Ancona, Italy

[8]Department of Chemistry, The University of Hong Kong, Hong Kong, China

[9]Hong Kong Quantum AI Lab, Hong Kong, China

[10]Chemistry Department, Sapienza University of Rome, Rome, Italy

Correspondence
Jian Wang and Stefano Passerini, Karlsruhe Institute of Technology (KIT), Karlsruhe D76021, Germany.
Email: jian.wang@kit.edu and stefano.passerini@kit.edu

Hongzhen Lin, i-Lab & CAS Key Laboratory of Nanophotonic Materials and Devices, Suzhou Institute of Nano-Tech and Nano-Bionics, Chinese Academy of Sciences, Suzhou 215123, China.
Email: hzlin2010@sinano.ac.cn

Abstract

Low-temperature zinc batteries (LT-ZIBs) based on aqueous electrolytes show great promise for practical applications owing to their natural resource abundance and low cost. However, they suffer from sluggish kinetics with elevated energy barriers due to the dissociation of bulky $Zn(H_2O)_6^{2+}$ solvation structure and free Zn^{2+} diffusion, resulting in unsatisfactory lifespan and performance. Herein, dissimilar to solvation shell tuning or layer spacing enlargement engineering, delocalized electrons in cathode through constructing intrinsic defect engineering is proposed to achieve a rapid electrocatalytic desolvation to obtain free Zn^{2+} for insertion/extraction. As revealed by density functional theory calculations and interfacial spectroscopic characterizations, the intrinsic delocalized electron distribution propels the $Zn(H_2O)_6^{2+}$ dissociation, forming a reversible interphase and facilitating Zn^{2+} diffusion across the electrolyte/cathode interface. The as-fabricated oxygen defect-rich V_2O_5 on hierarchical porous carbon (ODVO@HPC) electrode exhibits high capacity robustness from 25 to $-20°C$. Operating at $-20°C$, the ODVO@HPC delivers 191 mAh g^{-1} at

Jian Wang and Hongfei Hu contributed equally to this study.

50 A g^{-1} and lasts for 50 000 cycles at 10 A g^{-1}, significantly enhancing the power density and lifespan under low-temperature environments in comparison to previous reports. Even with areal mass loading of ~13 mg cm^{-2}, both coin cells and pouch batteries maintain excellent stability and areal capacities, realizing practical high-performance LT-ZIBs.

KEYWORDS

defect catalysis, delocalized electron engineering, diffusion kinetics modulation, low-temperature Zn batteries, V$_2$O$_5$ cathode

1 | INTRODUCTION

Impending environmental and climate concerns has initiated the pursuit for sustainable electrochemical energy storage solutions. Although lithium-ion batteries (LIBs) dominate the current portable and smart market due to their high energy density and extended cycle life, the utilization of scarce resources as well as the reliance on flammable liquid electrolytes hinders their applicability in terms of environmental-friendliness, affordability and safety.[1] Recently, zinc batteries (ZIBs) employing insertion cathodes and based on aqueous electrolyte have exhibited unparalleled advantages in terms of high theoretical capacity (820 mAh g^{-1}, based on Zn), low cost, superior safety and the low redox potential of zinc (−0.763 V vs. standard hydrogen electrode).[2-5] Cathode development of materials such as metal oxide,[6] sulfide,[7] and Prussian blue[8] by rational designs has achieved high energy density. However, their cycling or rate performances and lifespan are far from satisfactory especially when cycled under low-temperature surroundings. Such systems suffer from the following challenges[9-16]: (i) severe Zn^{2+} solvation in bulky electrolyte, lowering the diffusion rate and contributing to huge desolvation and diffusion barriers; (ii) the relatively strong Zn^{2+}-solvents binding affinity, impeding the formation of bare Zn^{2+} for intercalating and diffusing in the cathode, and causing co-intercalation of solvents or proton; (iii) the unstable and irreversible cathode electrolyte interphase (CEI), deteriorating the performance of ZIBs.

To resolve these existing problems, current strategies focus on tuning electrolyte compositions or altering Zn^{2+} solvation shells through introducing various organic reagents that is, polycarbonate (PC), N-methylpyrrolidone (NMP)[17-19]; or adopting "water-in-salt" to form high concentration electrolytes.[20,21] However, these approaches only target the physical solvation structures of aqueous bulky electrolytes, burdening the cost of aqueous batteries owing to the excessive usage of organic additives and sacrificing the rate performance. Another method is enlarging the layer spacing of active

materials by elemental metal doping.[22-24] While the widened layer spacing can facilitate the mobility of the large Zn(H$_2$O)$_x^{2+}$ complex to enter the crystalline structure, it still has to overcome the large diffusion barrier caused by the steric hindrance and increased intermolecular interactions under low-temperature environment (Figure 1A).[25] In addition, it is postulated that layer spacing engineering cannot resolve the desolvation of Zn(H$_2$O)$_x^{2+}$, inducing the co-insertion of solvents and consuming electrolytes. As solvated larger Zn(H$_2$O)$_x^{2+}$ are deemed to encounter much higher intercalation and diffusion barriers in the cathode than free Zn ones, desolvation becomes the prerequisite step before the zinc ions enter the solid phase, which should occur at the cathode/electrolyte interface, becoming the rate-determining step (Figure 1A).[26-31] Meanwhile, under low-temperature surroundings, the solvation phenomenon of hydrated zinc ions is more severe in comparison to that at room temperature owing to the freezing solidification of electrolyte resulting from the hydrogen bond network.[32,33] Therefore, finding an effective method to decrease the desolvation barrier is requisite to enhance the Zn^{2+} transfer and transport kinetics at low temperatures.

Recently, spin electron state modification is anticipated to generate more active sites to optimize the electrocatalytic activity. Defect engineering is feasible to modulate intrinsic physiochemical properties of electrode materials by breaking the lattice symmetricity, providing abundant active sites.[31,34-38] As expected, the existence of oxygen defects in metal oxides can decrease the insertion/extraction reaction barriers, realizing rapid diffusion paths and propelling the ion exchange kinetics across the interface or in the interior.[39] Nonetheless, there is seldom knowledge regarding low-temperature Zn batteries (LT-ZIBs) where the main factors affecting the internal reaction have shifted from the electrolyte to the interfacial ion diffusion, along with the desolvation effect for free ions.[40-43] Regardless of electrolyte engineering modification, prior to the freezing point of normal aqueous electrolyte, the low-temperature performance of Zn-V$_2$O$_5$
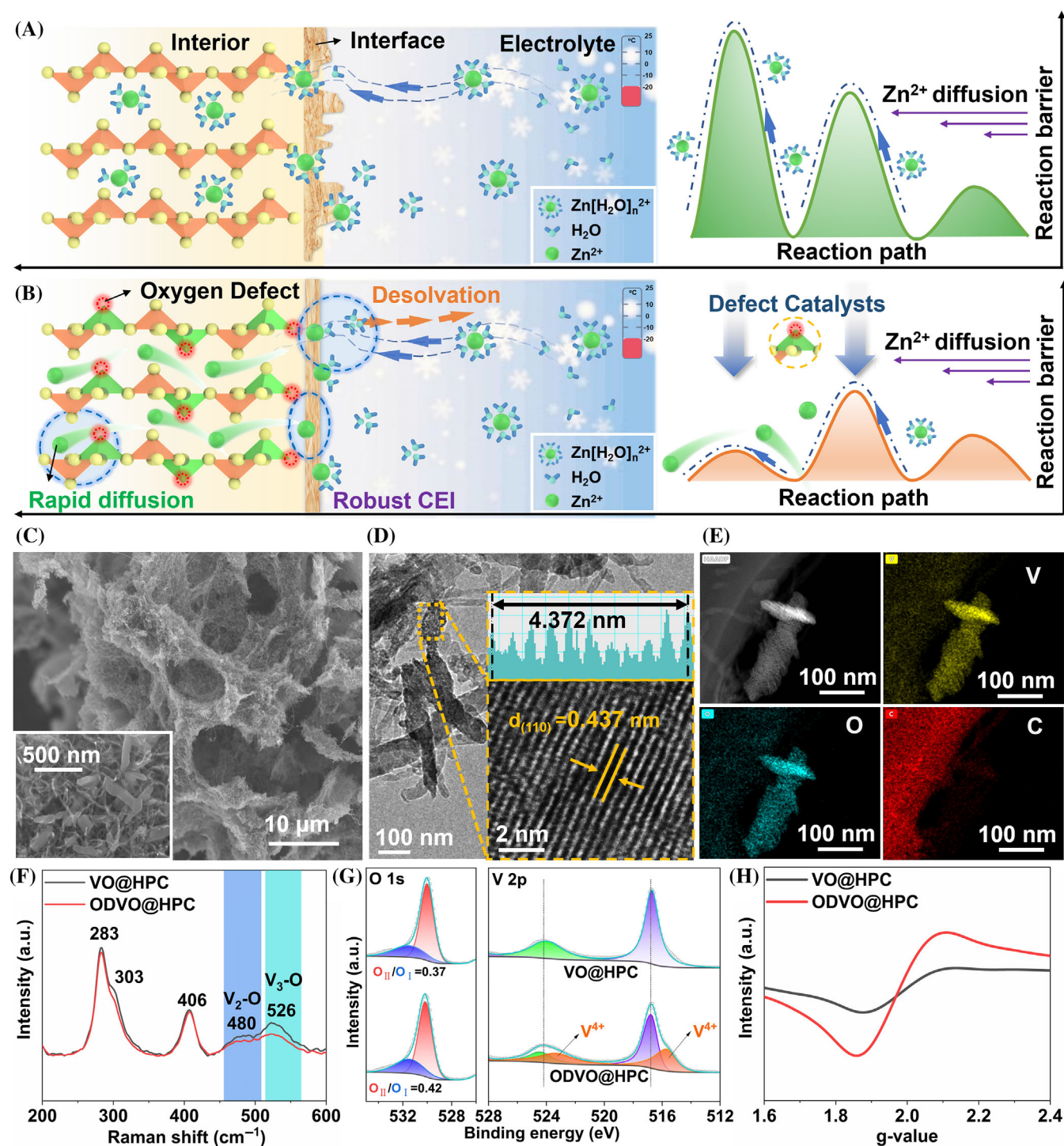
FIGURE 1 Schematic illustration, synthesis, and characterizations of the ODVO@HPC. Schematic illustration of the Zn behavior at the cathode interface and interior diffusion on (A) the pristine VO with large desolvation and diffusion barriers or (B) defect-rich ODVO with low desolvation/diffusion barriers under low-temperature environments. (C) Low- and high-resolution SEM images and (D) high-resolution TEM images of the as-synthesized ODVO@HPC nanocomposites; (E) corresponding EDS elemental mapping images of V, O and C in ODVO@HPC. (F) Comparison of VO@HPC and ODVO@HPC Raman spectra; (G) comparison of O 1s and V 2p regions in the VO@HPC and ODVO@HPC high-resolution XPS spectra; (H) comparison of VO@HPC and ODVO@HPC EPR spectra.

cells is still unknown. In our previous studies of Li metal batteries, we had identified that the optimization of the electronic state served as an electrocatalyst accelerates the desolvation process for generating bare Li ions/atoms.[44–48] The catalytic desolvation strategy is based on the dissociation behavior of $Zn(H_2O)_x^{2+}$ complex,

displaying the beneficial features of high efficiency and selective catalysis. Therefore, delocalizing electrons through defect engineering has great potentials to offer both fast interior reaction kinetics and enhanced interface desolvation capabilities for achieving high-performance LT-ZIBs.

Herein, differing from electrolyte tuning, layer spacing enhancement architecture or pore sieving strategy, delocalized electrons in cathode materials through constructing intrinsic defect engineering is performed to dissociate hydrated $Zn(H_2O)_x^{2+}$ complex for fast free ion diffusion to achieve ultra-high rate performance and record-level lifespan of LT-ZIBs. As a prototype, oxygen-defective V_2O_5 supported on hierarchical porous carbon (ODVO@HPC) is fabricated, which not only accelerates the desolvation kinetics of $Zn(H_2O)_x^{2+}$, but also promotes the reversible transport of Zn^{2+} across the CEI and in the cathode interior at low temperatures, as confirmed by X-ray measurements, interface-sensitive sum frequency generation (SFG) spectroscopy, and time-of-flight secondary-ion-mass-spectrometry (TOF-SIMS). Owing to the improved Zn^{2+} kinetics, the fabricated ODVO@HPC cathode exhibits capacity robustness in a wide environmental temperature, ranging from 25 to $-20°C$. Under $-20°C$, the ODVO@HPC cathode delivers a capacity of 470 mAh g^{-1} at 0.5 A g^{-1} and remains 191 mAh g^{-1} even at an ultrahigh rate of 50 A g^{-1}. Also, the cell stabilizes a capacity of 233 mAh g^{-1} at 10 A g^{-1} with a record-level long lifespan of 50 000 cycles. Enlarging mass loading to ~13.7 mg cm^{-2}, the prepared pouch cell shows an outstanding area capacity of 3.4 mAh cm^{-2}, highlighting the possibility of achieving high-performance LT-ZIBs.

2 | RESULTS AND DISCUSSION

2.1 | Preparation and characterization of ODVO@HPC with oxygen vacancies

As illustrated in Figure 1A, before intercalation, the diffusion of hydrated $Zn(H_2O)_x^{2+}$ complex encounters very high desolvation and diffusion energy barriers due to the steric effect, leading to ultralow mobility at low temperatures,[13,31] becoming the prerequisite and rate-determining step. The relatively strong binding between Zn^{2+} and related surrounding water molecules contributes to the huge desolvation barrier at the electrode/electrolyte interface, which severely limits the transfer of Zn^{2+} at decreased temperatures.[17,28,49] Our recent works confirm the interfacial desolvation and diffusion barriers can be considerably reduced by introducing active catalysts.[50–52] As a result, the hydrated $Zn(H_2O)_x^{2+}$ complex is rapidly dissociated to form free Zn^{2+} once reaching the electrocatalytic surface, leaving the free H_2O in the electrolyte (Figure 1B). Meanwhile, the smaller size of free Zn^{2+} can diffuse through the interphase and into the ODVO interior smoothly without any destruction. In sharp contrast, the co-intercalation of the solvent molecules or proton (H^+) together with the partially dissociated $Zn(H_2O)_x^{2+}$ in the layer spacing of the cathode interface will distort the crystalline structure and form undesired harmful H_2 gas, deteriorating the stability of the electrode.[53] Owing to the high activity of interfacial catalysis by lowering internal reaction barriers, the diffusion kinetics of Zn^{2+} is uniformized for the ODVO@HPC electrode, forming a continuous robust CEI layer.

The generation of delocalized electrons in ODVO@HPC was performed by H_2 reduction to form more defects. Briefly, the metal precursor ions are initially adsorbed on hybrid carbon and then converted to VO@HPC after treatments. Successively, under the reductive H_2/Ar atmosphere, the active ODVO@HPC was obtained by removing some oxygen atoms from the lattice sites of VO, delocalizing intrinsic electron distribution. In comparison to the VO@HPC (Figure S1), the obtained scanning electron microscope (SEM) image of ODVO@HPC reserves the cross-linked morphology with hierarchical pores and the V_2O_5 nanorods are interwoven on the matrix (Figure 1C), providing the effective pathways for Zn^{2+} and electron transport.[46,54] In the high-resolution transmission electron microscope (HR-TEM) images, consistent with the SEM results, both the VO@HPC and ODVO@HPC display the porous morphology. However, the assigned (110) interplanar spacing distance is slightly expanded from 0.423 to 0.437 nm (Figure 1D and S2), indicating the success of modulating electron states.[55] Meanwhile, all the elements including C, V, and O are uniformly distributed in ODVO@HPC as confirmed by the energy dispersive spectroscopy (EDS) mapping results (Figure 1E).

To demonstrate the delocalized electrons constructed by oxygen defects, X-ray diffraction (XRD), Raman spectroscopy, X-ray photoelectron spectroscopy (XPS), and electron paramagnetic resonance (EPR) measurements were performed together with the above-mentioned TEM. Compared with VO@HPC (JCPDS No. 77–2418), the peak intensity of (110) crystal facet is reduced and shifted in the ODVO@HPC sample (Figure S3A).[45] Both of the two samples exhibit similar Raman peak signals (Figures S3B and 1F). However, the characteristic peaks at 480 and 526 cm^{-1} ascribed to V_2-O and V_3-O stretching vibration bonds are slightly weakened after reduction, implying the V-O bond is affected by neighboring oxygen defects.[56,57] In the high-resolution XPS spectrum of O 1 s, two peaks at 530.4 (O_I) and 531.4 eV (O_{II}) are ascribed to the lattice oxygen and defective

oxygen (Figure 1G), respectively, and the increased ratio of defective oxygen from 0.37 to 0.42 indicates the presence of abundant oxygen defects in the ODVO@HPC.[46] In spite of the original V^{5+}, the new peak signals at 515.3 and 523.3 eV are evident as the formation of V^{4+} resulting from the effect of oxygen defects.[58] In relation to the VO@HPC, ODVO@HPC has a stronger peak intensity at $g = 1.97$ (Figure 1H), attributing to the increased number of unpaired electrons generated from the synergistic formation of oxygen vacancies and the relevant valence state variation of V^{4+} after hydrogen reduction.[59] The formation of V^{4+} complex creates an electron delocalized field, which is beneficial to form more catalytic sites to drive the dissociation of the solvated $Zn(H_2O)_6^{2+}$ ions at the electrode/electrolyte interface. These results demonstrate the success of introducing intrinsic oxygen defects into the cathode system with slight changes of the V valence state, which synergistically delocalizes surrounding electron states and participate in the catalytic reaction. As estimated in the thermogravimetric analysis (TGA), the ODVO accounts for ∼76 wt.% in the nanocomposites (Figure S4A).

2.2 | Record-level lifespan and ultrahigh-rate performances of LT-ZIBs

To investigate the catalytic effects on dissociating $Zn(H_2O)_x^{2+}$ complex in LT-ZIBs by delocalized electrons, the electrochemical performances of VO@HPC and ODVO@HPC cathodes were compared based on conventional 3 mol L^{-1} $Zn(CF_3SO_3)_2$ aqueous electrolyte with the freezing point as low as $-26.4°C$ (Figure S4B). To signify the hard solvation and diffusion without catalysts, the working temperature was set at $-20°C$ and any improvement must be ascribed to the enhanced kinetics in desolvation and diffusion catalyzed by the surface electronic density modulation for more active sites. Ideally, practical batteries should function in varying climates over a wide temperature range. As displayed in Figures 2A and S5, the ODVO@HPC electrode displays the capacity of 491 mAh g^{-1} at 25°C while it maintains the capacity retention of 82.3% at 5 A g^{-1} after decreasing the surrounding temperature to $-20°C$, much higher than the controlled one (352 mAh g^{-1} for VO@HPC at $-20°C$). To demonstrate the intrinsic catalysis in decreasing the desolvation barriers, the following electrochemical tests were performed under $-20°C$. Two pairs of redox peaks between 0.2 and 1.6 V exist in both the ODVO@HPC and VO@HPC electrodes, indicating the multi-steps of intercalation/extraction reaction (Figure S6).[55,60] However, the ODVO@HPC electrode shows narrower voltage gap and higher current peak and

area than the controlled VO@HPC electrode, demonstrating the faster Zn ion dissociation/diffusion kinetics. When cycled at 0.5 or 5 A g^{-1}, the ODVO@HPC stabilizes the capacity with high Coulombic efficiency and low voltage gap (Figure S7). For example, at 5 A g^{-1} (Figures 2B and S8), the ODVO@HPC maintains a capacity retention of 92.5% after 1500 cycles. More importantly, the ODVO@HPC electrode outputs the specific capacities of 456, 428, 386, 248 and 191 mAh g^{-1} at 2, 5, 10, 30 and 50 A g^{-1}, respectively. Switching back to 1 A g^{-1}, ODVO@HPC recovers the capacity of 467 mAh g^{-1} (Figure 2C), nearly the original capacity, implying high reversibility and stability. In contrast, as revealed by the voltage curves (Figure S9), depressive desolvation kinetic reactions with high polarization are exhibited in the VO@HPC. Compared to the state-of-the-art ZIBs under low-temperature environment, we observe ODVO@HPC is capable of providing a high energy density of 421 Wh kg^{-1} at 1 A g^{-1} and excellent ultra-high power density of 45 kW kg^{-1} (Figure 2D), which has yet to be reached in the LT-ZIBs.[9,11,12] In the long-term cycle, the ODVO@HPC electrode is capable of delivering an initial high capacity of 388 mAh g^{-1} and surviving for 50 000 cycles (about 104 days) at 10 A g^{-1} (Figure 2E). Even though the capacity retention is decreased to 60% after 50 000 cycles, the net specific capacity value of 233 mA h g^{-1} is still achieved, further indicating the robust structure of cathode during the cycling test. Compared with other reported ZIBs at room temperature, the lifespan and specific capacity of ODVO@HPC is superior (Figure 2F and Table S1).[9,61–74] During this period, the cathode maintains a stable capacity even after a long-term cycle of 30 000 cycles, showing the robust ability in resisting self-discharge. The slight capacity improvement after 30 000 cycles is attributed to further insertion of the surface remaining unreacted Zn^{2+} into the ODVO@HPC electrode at ultra-high current density after the intentional rest of the battery. These significantly enhanced electrochemical performances at various current densities under low temperature of $-20°C$ confirm the benefit of accelerated desolvation kinetics by intrinsic catalysis forming bare Zn ions and promoting Zn ion transport in the ODVO interior.

2.3 | Improved Zn kinetics investigated by electrochemical and theoretical methods

To probe the delocalized electrons on intrinsic catalytic functions of defects in relation to accelerate $Zn(H_2O)_x^{2+}$ desolvation and ameliorate the Zn ion kinetics, along with the increase of scanning rates, the currents of redox
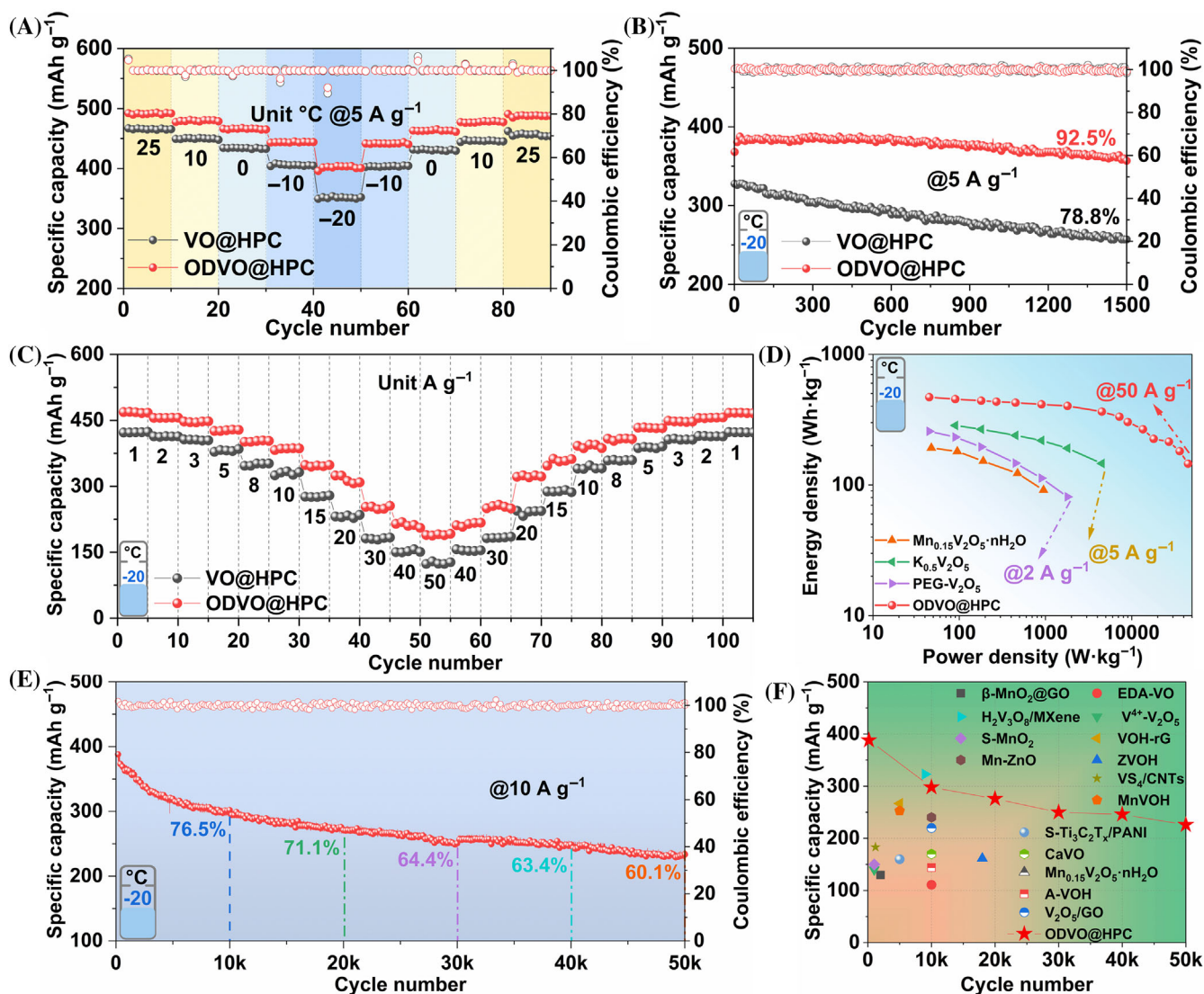
FIGURE 2 Record-high cycling and rate performances of LT-ZIBs based on ODVO@HPC cathodes. (A) Cycling performance of the two electrodes at 5 A g^{-1} in a wide temperature range from 25 to −20°C; (B) comparison of cycling performance at 5 A g^{-1} and (C) rate performance up to 50 A g^{-1} at −20°C. (D) Comparison of power density and energy density between our study and previously reported LT-ZIBs; (E) ultralong cycling lifespan of the ODVO@HPC electrode at high current density of 10 A g^{-1} under −20°C; (F) comparison of long lifespan and capacity between our study and previously reported room temperature batteries.

peaks are enhanced, and the redox peak voltage shifts slightly (Figures 3A and S10A). Based on the equation of $\log(i) = b \log(v) + \log(a)$, the calculated b value is larger than 0.5, indicating the reaction process is capacitive-controlled (Figure S10B,C).[75] In addition, as summarized in Figure 3B, the ODVO@HPC electrode exhibits higher contribution than the VO@HPC electrode in diffusion. For example, at 0.4 mV s^{-1}, the capacitance contribution accounts for 93.9% of the total Zn^{2+} storage (Figure S10D). According to the classic Randles-Sevcik equation, the ODVO@HPC electrode displays five times higher in Zn^{2+} diffusion coefficients than the controlled VO@HPC in both the charge and discharge states (Figures 3C, S11, and Table S2), suggesting the much

lower desolation and diffusion barriers that must be overcome at the interface and interior.[76] The cell with catalytic sites shows a charge transfer resistance of ~225 Ohm, which only accounts for less than one third in the pristine one (740 Ohm). At the same time, after initial activation, both the charge transfer resistance was decreased, but the ODVO@HPC electrode still showed the lower resistance, indicating the fast charge transfer kinetics propelled by the formed catalytic sites, as demonstrated by electrochemical impedance spectroscopies in Figure S12.[77]

Further, the binding ability and diffusion barriers of free Zn ions on the VO and ODVO were computed using density functional theory (DFT) calculations
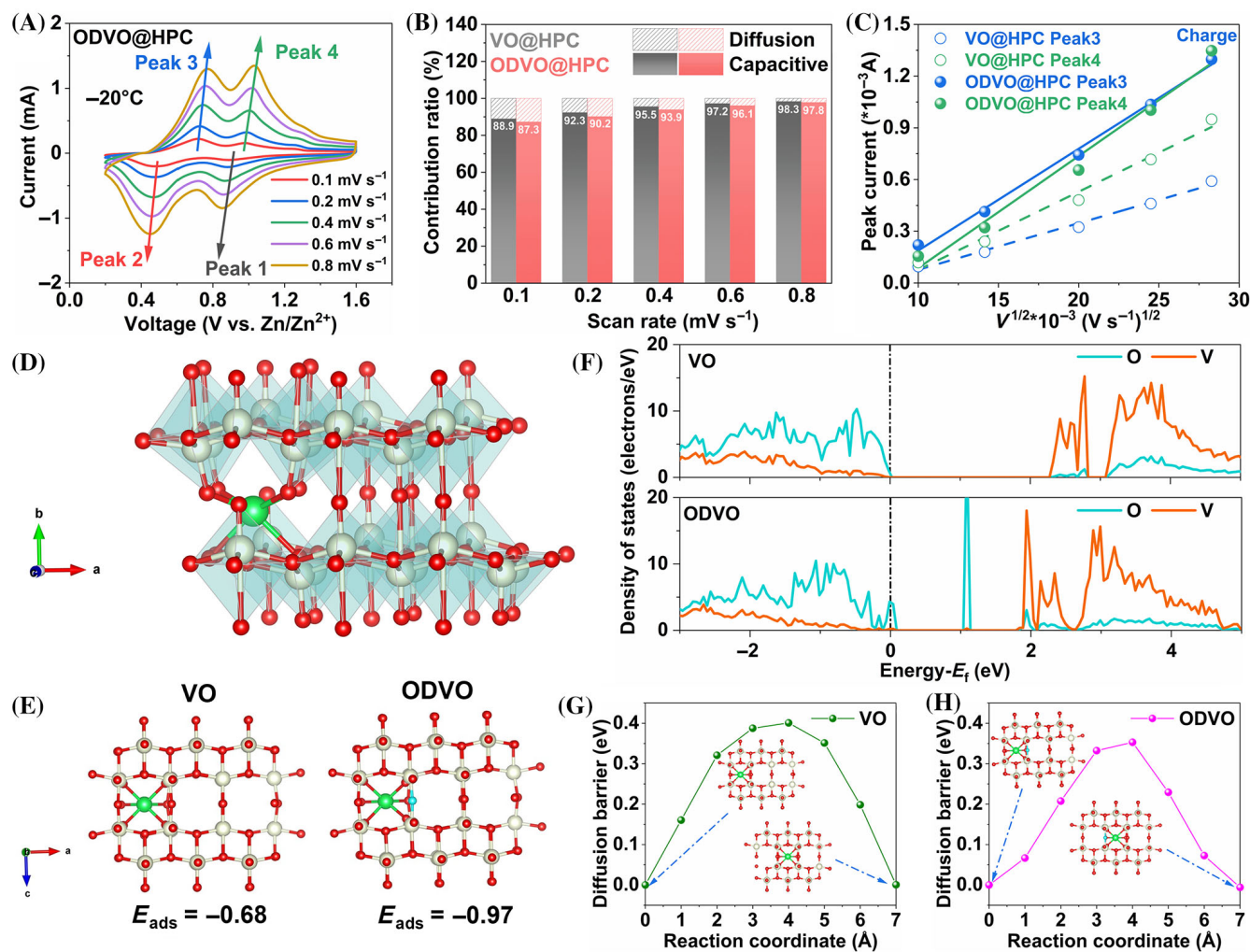
FIGURE 3 Investigation of the kinetics revealed by electrochemical and theoretical methods. (A) CVs at different scan rate from 0.1 to 0.8 mV s^{-1}; (B) percentage contribution of diffusion to total capacity; (C) peak current versus $\nu^{0.5}$ plots of four peaks in CVs at charge state. The white, green and red balls represent the V, Zn and O atoms; (D) Schematic illustration of Zn-ion intercalation in VO; the oxygen atom that is removed for constructing the vacancy defects are depicted as cyan balls; (E) comparison of Zn-ion intercalation in VO and ODVO and (F) the electronic density of states (DOS) for VO and ODVO; the energy barriers for Zn-ion migration in (G) VO and (H) ODVO.

(Figure 3D–H). The schematic illustration of Zn^{2+} intercalation is depicted in Figure 3D, and the free Zn ions were adsorbed in the layer structure of VO with/without oxygen vacancies.[78,79] In comparison with the pristine perfect VO, the surface with delocalized electrons exhibited stronger capability toward Zn^{2+} and the calculated binding energy was significantly increased from 0.68 for VO to 0.97 eV for ODVO (Figure 3E). The Fermi level (E_f) of the pristine VO are located at the valence-band maximum in the density of states (DOS), whereas the introduction of intrinsic defects induced the shifting of E_f toward the valance-band, indicating that the oxygen defects are capable of promoting the rearrangement of internal electrons and improving the electrical conductivity for superior intercalation (Figure 3F).[70,80] In addition, the barriers of Zn ion migration diffusing along layer

spacing in the VO and ODVO were explored. In contrast to VO, the diffusion energy barriers were decreased from 0.4 to 0.35 eV, corresponding to the reduction energy of 4824 J mol^{-1} (Figure 3G,H). Therefore, we can conclude that the defects in ODVO are able to delocalize electron distribution to enhance the capability in accelerating Zn(H$_2$O)$_x^{2+}$ desolvation, Zn ion storage and diffusion.

2.4 | Interfacial desolvation and diffusion evolution elucidated by spectroscopic characterizations

The electrochemical performances are related to the behaviors of Zn^{2+} desolvation and diffusion kinetics across the interface and in the interior. Owing to the
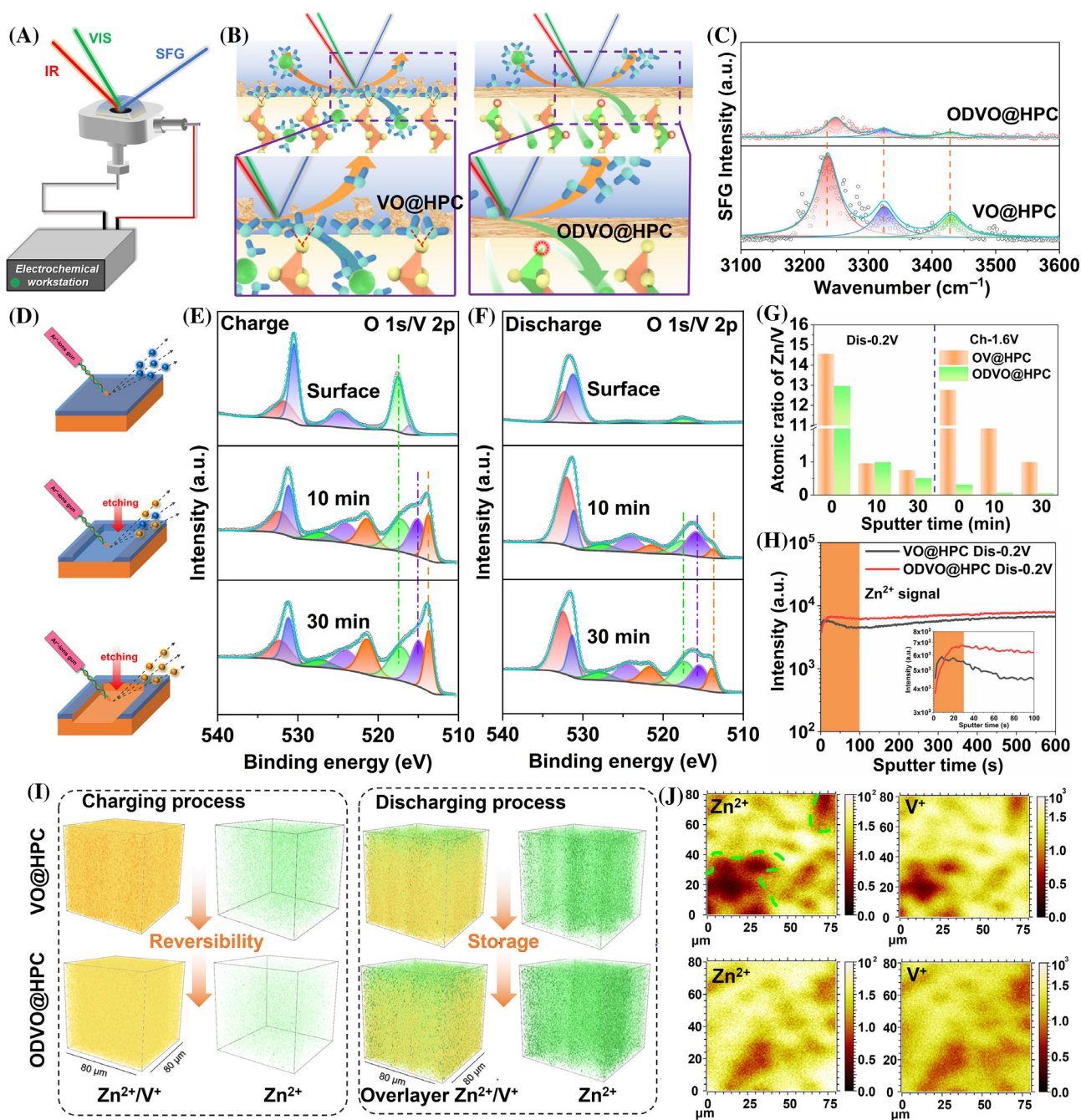
FIGURE 4 Interfacial evolutions visualized by SFG, in-depth XPS and TOF-SIMS. (A) Schematic diagram of in situ SFG and (B) solvation/desolvation diagrams at the interface; (C) SFG spectrum of —OH signals at 3100–3600 cm^{-1}. (D) Illustration of in-depth XPS deep-profile mechanism; the evolutions of O 1s/V 2p spectra in the cycled ODVO@HPC cathodes after (E) fully charging and (F) fully discharging processes; (G) corresponding summary of the Zn/V atom. (H) Intensity comparison of Zn^{2+} species in cycled VO@HPC and ODVO@HPC cathodes at full discharge to 0.2 V; (I) 3D reconstructions and (J) top-view surface mappings of Zn^{2+} and V^{+} species in VO@HPC and ODVO@HPC at fully discharging/charging states, respectively.

desolvation behavior that takes place at the electrode/electrolyte interface, the in situ interface-sensitive vibrational SFG spectroscopy was configured and applied to observe electrode/electrolyte interface variation and monitor the electrocatalysis toward hydrate Zn(H$_2$O)$_x$$^{2+}$ species dissociation (Figure 4A–C).[81,82] In the in-situ cell

(which has a similar configuration to a coin cell), the working electrode and counter electrode are ODVO@HPC (VO@HPC) and Zn metal, respectively, as depicted in Figure 4A. The water molecules at the interface exhibit different behaviors on the two electrode surfaces (Figure 4B). Strong solvent signals of water located

at 3236, 3324 and 3431 cm^{-1} were evidenced at the electrolyte interface (Figure 4C).[83] However, after introducing interfacial catalysis into the system, the intensities of —OH signals become much weaker, suggesting most of the water molecules were dissociated from the $Zn(H_2O)_x^{2+}$ complex. As applying bias voltage on the electrode/electrolyte interface, the catalytic sites accelerate the weakened coordination to break down to release Zn^{2+} and H_2O molecules from the hydrate $Zn(H_2O)_x^{2+}$. The released H_2O molecules are repelled by the interface back to the electrolyte phase, causing desorption, decreasing SFG signal intensity and leaving the formation of free Zn ions. Figure 4D illustrates the schematics of the cycled electrodes etched by Ar^+ gradually, and the corresponding signals are collected from surface to interior. In comparison to the initial state without any etching, more V-based signals at 513.6, 516.4 and 517.1 eV arise either in the fully charging or discharging state after etching, implying the formation of CEI on the electrode (Figure 4E,F).[24,77] The quantifications of atomic percentages are summarized, and the corresponding atomic Zn/V ratio displays a decreasing trend in the fully charging/discharging states. In contrast to the same state, that is, etching for 30 min, the ODVO@HPC has a higher and stronger signal before and after Zn^{2+} intercalation/extraction than VO@HPC (Figure S13), which is the main reason it exhibits higher capacity retention rate and ultralong lifespan. The apparent difference is that the ODVO@HPC possesses the weaker residual Zn^{2+} signal in the electrode after full extraction compared with VO@HPC (Figure 4G), indicating the reversibility of the formed CEI as reflected in the cross-sectional SEM images in Figure S14. Such repeating formation/decomposition of CEI process will turn over the active sites for smooth desolvation. The surface information and species distribution in the CEI or interior were well-reconstructed via TOF-SIMS. When fully discharged, the VO@HPC electrode displayed the higher intensity of Zn^{2+} species at the initial 150 s (Figure 4H), indicating more Zn^{2+} reserved in the CEI layer. Later, the Zn^{2+} signal in the ODVO@HPC is stronger than the controlled one, while under fully charged state, the intensity of Zn^{2+} signal in ODVO@HPC is much weaker than that in VO@HPC (Figure S15), denoting the excellent storage and reversibility of Zn ions in the electrode. In addition, Figure 4I exhibited the species distributions of zinc and vanadium in the electrodes. Upon charging, the Zn^{2+} extracts from the electrode interior and across the CEI layer to transfer into electrolyte. The left remained Zn^{2+} signal should be ascribed to the "dead" Zn in the cathode. The dark green intensity indicates more Zn^{2+} storage in the cathode. Both electrodes have very strong Zn^{2+}

signals when Zn is intercalated, while the ODVO@HPC exhibited weak Zn^{2+} signal after extraction, consistent with the in-depth XPS results, indicating superior reversibility due to the presence of the interfacial catalyst in the ODVO@HPC.[84] In sharp contrast, the Zn and V species are uneven on the VO@HPC surface, as highlighted by the green line (Figure 4J), severely hindering the reversibility and utilization. These results imply that the delocalized electron engineering via surface oxygen defects promotes the Zn kinetics to diffuse smoothly across the interface and in the interior.

2.5 | Large-scale high-loading low-temperature pouch cells

To assess potential application, high-loading batteries were assembled and assessed at the low temperature of $-20°C$. All cells stabilize the capacities without any loss during the 100 cycles even when increasing the loading from 5.0 to ~8 mg cm^{-2} (Figures 5A and S16). For example, the cell with 5.0 mg cm^{-2} delivers the average capacity of 389 mAh g^{-1} and maintains the capacity retention of 98.9% after 550 cycles (Figure 5B). In addition, as illustrated in Figure 5C, the fabricated large-sized pouch cells can power the Christmas tree consisting of shaped LED lights at $-20°C$ (Figure 5D). With an ultrahigh areal loading of 13.7 mg cm^{-2}, the pouch cell with the N/P mass ratio of 5:1 was assembled, where the excessive Zn metal (100 μm) acts as the current collector as well. Cycled at 1.67 mA cm^{-2}, the low-temperature pouch cell provides a specific capacity of 260 mA h g^{-1}, corresponding to 3.6 mA h cm^{-2} and 125 Wh kg^{-1} based on the cathode. After 100 cycles, it can stabilize ~3.4 mAh cm^{-2} (Figure 5E), which meets the demands of Li batteries. In addition, the strategy of forming delocalized electrons to generate catalytic functions through surface defect engineering can be extended to other cathodes such as MnO_2. Under the low-temperature of 0°C, the commercial MnO_2 electrodes with oxygen defects (ODMO@C) still exhibit the superior capacity enhancements in rate capacity up to 2 A g^{-1} and a stable lifespan of 500 cycles (Figure 5F,G), demonstrating the promising future of using defect engineering for fast desolvation and ion diffusion under low-temperature environments.

3 | CONCLUSION

In summary, a strategy of forming delocalized electrons to generate more active sites by defect engineering is proposed to accelerate the $Zn(H_2O)_x^{2+}$ desolvation at the
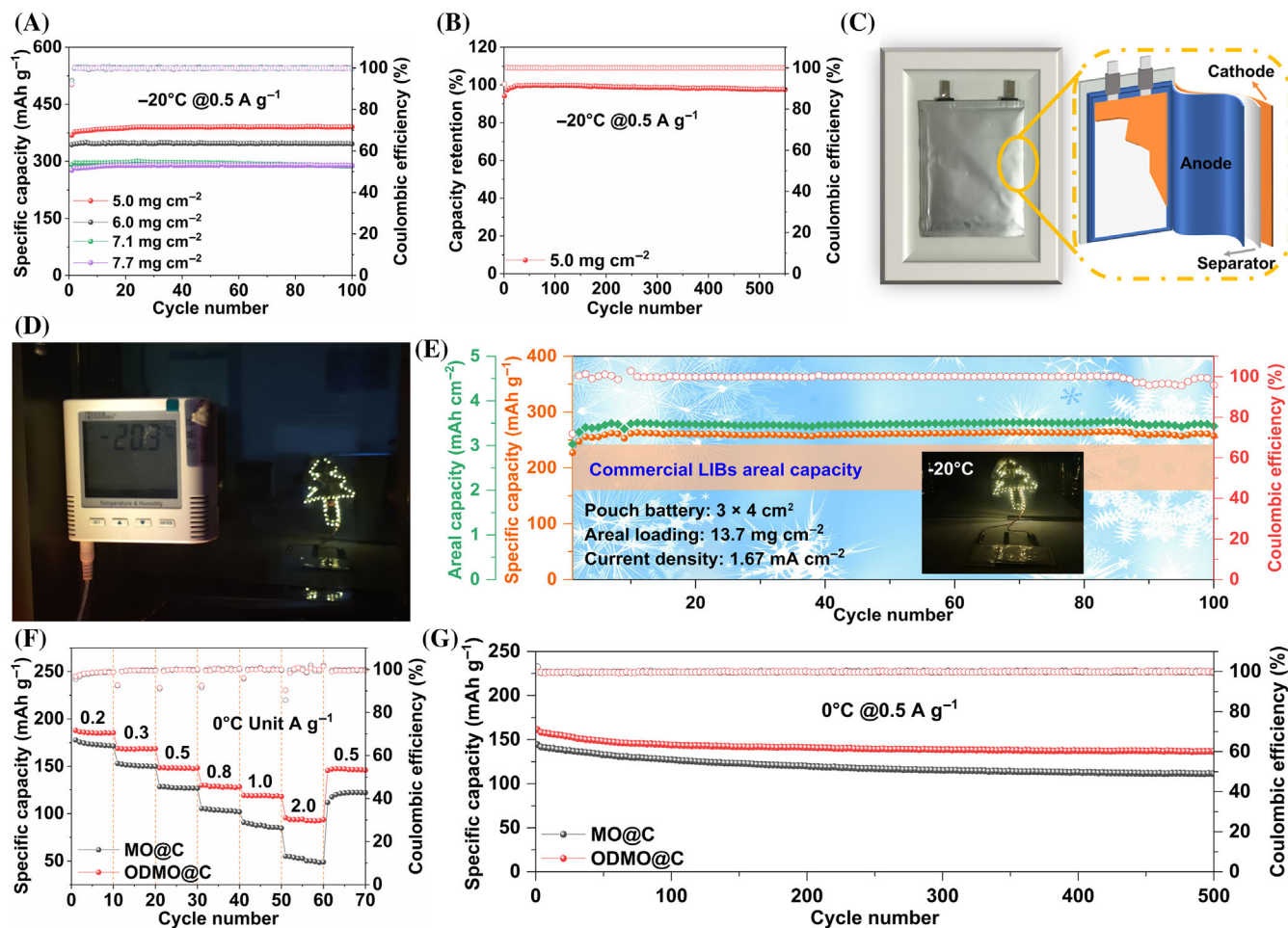
FIGURE 5 High loading coin/pouch cells based on ODVO@HPC or oxygen-vacant ODMO@C cathode. (A) Cycling performance of high loading cells at 0.5 A g^{-1} from 5.0 to 7.7 mg cm^{-2} under −20°C; (B) capacity retention within 550 cycles at 0.5 A g^{-1} under −20°C; (C) Illustration and optical images of pouch cell; (D) image of a Christmas tree light powered by pouch cells at −20°C; (E) cycling performance of high areal loading pouch battery under 13.7 mg cm^{-2} at 1.67 mA cm^{-2}. Electrochemical performances of MO@C and ODMO@C cathodes. (F) Rate performance from 0.2 to 2.0 A g^{-1} under 0°C; (G) Cycling performance at 0.5 A g^{-1} under 0°C.

electrode/electrolyte interface and Zn^{2+} diffusion kinetics in metal oxide cathode interior for low-temperature applications. As demonstrated by a comprehensive series of electrochemical measurements, spectroscopical characterizations and theoretical calculations, the formed oxygen defects can effectively reduce the barriers of desolvation and diffusion for sharply increased diffusion kinetics. Consequently, the defect-rich ODVO@HPC exhibits superior performances at varying temperatures. Specifically, the ODVO@HPC can store the capacity of 470 mAh g^{-1} at 0.5 A g^{-1}, 191 mAh g^{-1} at an ultrahigh current density of 50 A g^{-1} and last for 50,000 cycles with a capacity retention of 60.1% at 10 A g^{-1} under −20°C, outperforming the current state-of-the-art. The high loading pouch cell displays excellent stability and areal capacity in the long-term cycles, underlining the potential application of LT-ZIBs in harsh low-temperature environments.

4 | EXPERIMENTAL SECTION

4.1 | Material synthesis

Graphene oxide (GO) aqueous solution was achieved according to the improved Hummers' method. The GO aqueous solution (40 mL, 5 mg mL^{-1}) and carbon nanotubes powders (200 mg) were dispersed in 200 mL deionized water and sonicated for 45 minutes to obtain homogeneous suspension (Solution 1). The ODVO@HPC nanocomposite was achieved via hydrothermal and thermal reduction treatment. In a typical synthesis, 4.396 mmol of NH$_4$VO$_3$ powder was dissolved in ethylene glycol (40 mL) and kept at pH = 2–3 with diluted hydrochloric acid. Further, the solution was stirred for 90 minutes until it became an orange-yellow solution (Solution 2). The Solution 2 was slowly dropped into the above-prepared carbon suspension under stirring before

transferring into four 100 mL Teflon-lined autoclaves, and kept at 180°C for 24 h. The solid samples were collected after filtering, washing and then freeze-drying for 24 h. The obtained composite was annealed at 350°C for 2 h under air atmosphere with a heating rate of 4°C min^{-1} and then the VO@HPC was yielded after cooling down to room temperature. To introduce the oxygen defects, the composites were heated to 400°C for 1 h with a heating rate of 4°C min^{-1} under the atmosphere of H$_2$/Ar mixture, obtaining the ODVO@HPC nanocomposites. Similarly, the commercial MnO$_2$ was heated to 150°C for 1 hour with a heating rate of 4°C min^{-1} under the atmosphere of H$_2$/Ar mixture to obtain the MnO$_{2-x}$.

4.2 | Materials characterization

The porous morphology and structure of OV@HPC and ODVO@HPC were investigated by a field-emission scanning electron microscope (SEM, Hitachi Regulus 8230) and a F20 S-Twin field-emission transmission electron microscope (TEM, Tecnai G2). X-ray diffraction (XRD, Bruker D8) was adopted to characterize the crystal structure of as-synthesized composite material as well as the crystal plane spacing offsets. Raman spectra (Horiba LabRAM) was selected to detect the V-O stretching vibration signal in the composite materials. Thermogravimetric analysis (TGA) measurement based on a TG/DTA-6200 thermal analyzer was performed to evaluate the weight content of V$_2$O$_5$ in the composites from room temperature to 600°C with 10°C min^{-1} under dry air atmosphere. And the DSC (DSC, 200 F3) test of 3 mol L^{-1} (M) Zn(CF$_3$SO$_3$)$_2$ electrolyte is set from −60 to 20°C under nitrogen atmosphere with 5°C min^{-1}. X-ray photoelectron spectroscopy (XPS) data were collected in an ESCALAB 250XI (Thermo Scientific) spectrometer to detect the valence change of V and O. Electron paramagnetic resonance (EPR) measurement was performed using a Bruker spectrometer (EPR, JEOL-FA200) to verify the presence of oxygen defects at room temperature. The 3D and top-view structures and species distribution in the electrodes were performed on IONTOF-type TOF-SIMS. Cyclic voltammetry (CV) was investigated between 0.2 and 1.6 V (0.8–1.8 V for MnO$_2$//Zn) using a coin cell configuration on a VMP-3 electrochemical workstation. Electrochemical impedance spectroscopy (EIS) measurements were performed in the frequency range from 200 kHz to 100 mHz using the same electrochemical workstation. For In-depth XPS measurement, the coin cells were charged to 1.6 V and then discharged to 0.2 V at −20°C after 10 cycles of activation.

4.3 | Set-ups of in situ sum frequency generation

The commercial sum frequency generation (SFG) with the second-order non-linear technology ($\omega_{vis} + \omega_{IR} = \omega_{SFG}$) and a picosecond laser system is adopted in a copropagating configuration. The visible green light with incident angle of 60° is 532 nm, and the IR pulse with incident angle of 55° is adjustable ranging from 1000 to 4000 cm^{-1}. The energy of the two light beams is generally less than 200 mJ, which is hard to generate the photodamage effect for the samples. The polarization combination is typically *ssp-mode* (s-polarized sum frequency beam, s-polarized visible beam, and p-polarized IR beam). In the in-situ cell (similar configuration to coin cell), the working electrode and counter electrode are ODVO@HPC (VO@HPC) and Zn metal, respectively. For in-situ SFG measurements, while applying bias voltage with electrochemical workstation, the two lights directly reach the interface of the electrode/electrolyte and then the sum frequency light is generated and reflected to the detector.

4.4 | Electrochemical conversion and measurements

For all electrochemical measurements, 3 M Zn(CF$_3$SO$_3$)$_2$ dissolved in aqueous water was selected as the electrolyte, glass microfiber GF/B (Whatman) with a diameter 18 mm as the separator, and the zinc foil (thickness of 100 μm) with a diameter 15 mm as the anode. All coin cells were galvanostatically charged/discharged for 25 cycles at 5 A g^{-1} at 25°C for the activation, except for the CV, EIS and characterization tests. Then, all the cells were placed at −20°C for testing. The homogenous slurry was fabricated by mixing active material (70 wt.%), super P (20 wt.%) and polyvinylidene fluoride (PVDF, 10 wt.%) in *N*-methylpyrrolidone (NMP) before coating onto the carbon film (diameter 10 mm) or carbon cloth (diameter 15 mm), followed by vacuum drying at 60°C for 72 hours. The average areal loading of the composite material was ~1.5–2.0 or ~5.0–7.7 mg cm^{-2}. The pouch cell size is 3 × 4 cm^2, and the mass loading was ~13.7 mg cm^{-2}. The electrochemical performances of these cells were performed on a LAND CT2001A multichannel battery test system. For Zn//MnO$_2$ battery, 2 M ZnSO$_4$ with 0.2 M MnSO$_4$ was used as the electrolyte, the average areal loading of the MnO$_2$ material was ~1.0 mg cm^{-2}.

4.5 | Computational details

The density functional theory (DFT) calculations were performed using the DS-PAW software integrated in the Device Studio program, providing a number of functions for performing visualization, modeling and simulation. The projected augmented wave (PAW) method was used to describe the electron-ion interaction, and the generalized gradient approximation (GGA) with the Perdew–Burke–Ernzerhof (PBE) functional was adopted for the exchange-correlation energy, and the cutoff energy of 500 eV was used. A $4 \times 4 \times 3$ Monkhorst–Pack is used for the k-mesh sampling in the first Brillouin zone. Geometry optimization was repeated until the total energy change of each ionic step was less than 10^{-4} eV and the force on each atom is smaller than -0.02 eV Å^{-1}. The van der Waals interactions were described by the DFT-D3 empirical correction method. The barriers of Zn migration in the samples were calculated by the climbing-image nudged elastic band (CI-NEB) method.

CONFLICT OF INTEREST STATEMENT
The authors declare no conflict of interest.

DATA AVAILABILITY STATEMENT
The data that support the findings of this study are available from the corresponding author upon reasonable request.

ORCID
Jian Wang https://orcid.org/0000-0002-7945-0826
Stefano Passerini https://orcid.org/0000-0002-6606-5304

REFERENCES

1. Zhang J, He R, Jia L, et al. Strategies for realizing rechargeable high volumetric energy density conversion-based aluminum–sulfur batteries. *Adv Funct Mater*. 2023;33(48):2305674.
2. Song M, Tan H, Chao D, Fan HJ. Recent advances in Zn-ion batteries. *Adv Funct Mater*. 2018;28(41):1802564.
3. Ming J, Guo J, Xia C, Wang W, Alshareef HN. Zinc-ion batteries: materials, mechanisms, and applications. *Mater Sci Eng R Rep*. 2019;135:58-84.
4. Li C, Jin S, Archer LA, Nazar LF. Toward practical aqueous zinc-ion batteries for electrochemical energy storage. *Joule*. 2022;6(8):1733-1738.
5. Lei S, Liu Z, Liu C, et al. Opportunities for biocompatible and safe zinc-based batteries. *Energy Environ Sci*. 2022;15(12):4911-4927.
6. Nam KW, Kim H, Choi JH, Choi JW. Crystal water for high performance layered manganese oxide cathodes in aqueous rechargeable zinc batteries. *Energy Environ Sci*. 2019;12(6):1999-2009.
7. Tan Y, Li S, Zhao X, et al. Unexpected role of the interlayer "dead Zn^{2+}" in strengthening the nanostructures of VS_2 cathodes for high-performance aqueous Zn-ion storage. *Adv Energy Mater*. 2022;12(19):2104001.
8. Hurlbutt K, Wheeler S, Capone I, Pasta M. Prussian blue analogs as battery materials. *Joule*. 2018;2(10):1950-1960.
9. Geng H, Cheng M, Wang B, Yang Y, Zhang Y, Li CC. Electronic structure regulation of layered vanadium oxide via interlayer doping strategy toward superior high-rate and low-temperature zinc-ion batteries. *Adv Funct Mater*. 2019;30(6):1907684.
10. Zhao Y, Chen Z, Mo F, et al. Aqueous rechargeable metal-ion batteries working at subzero temperatures. *Adv Sci (Weinh)*. 2020;8(1):2002590.
11. Su G, Chen S, Dong H, et al. Tuning the electronic structure of layered vanadium pentoxide by pre-intercalation of potassium ions for superior room/low-temperature aqueous zinc-ion batteries. *Nanoscale*. 2021;13(4):2399-2407.
12. Lin C, Qi F, Dong H, et al. Suppressing vanadium dissolution of V_2O_5 via in situ polyethylene glycol intercalation towards ultralong lifetime room/low-temperature zinc-ion batteries. *Nanoscale*. 2021;13(40):17040-17048.
13. Liu Z, Luo X, Qin L, Fang G, Liang S. Progress and prospect of low-temperature zinc metal batteries. *Adv Powder Mater*. 2022; 1(2):100011.
14. Gao S, Li B, Tan H, et al. High-energy and stable subfreezing aqueous Zn-MnO$_2$ batteries with selective and pseudocapacitive Zn-ion insertion in MnO_2. *Adv Mater*. 2022;34(21):e2201510.
15. Kim W-Y, Kim H-I, Lee KM, et al. Demixing the miscible liquids: toward biphasic battery electrolytes based on the kosmotropic effect. *Energy Environ Sci*. 2022;15(12):5217-5228.
16. Jia L, Hu H, Cheng X, et al. Toward low-temperature zinc-ion batteries: strategy, progress, and prospect in vanadium-based cathodes. *Adv Energy Mater*. 2023;14(8):2304010.
17. Chang N, Li T, Li R, et al. An aqueous hybrid electrolyte for low-temperature zinc-based energy storage devices. *Energy Environ Sci*. 2020;13(10):3527-3535.
18. Liu DS, Zhang Y, Liu S, et al. Regulating the electrolyte solvation structure enables ultralong lifespan vanadium-based cathodes with excellent low-temperature performance. *Adv Funct Mater*. 2022;32(24):2111714.
19. Li TC, Lim Y, Li XL, et al. A universal additive strategy to reshape electrolyte solvation structure toward reversible Zn storage. *Adv Energy Mater*. 2022;12(15):2103231.

20. Lukatskaya MR, Feldblyum JI, Mackanic DG, et al. Concentrated mixed cation acetate "water-in-salt" solutions as green and low-cost high voltage electrolytes for aqueous batteries. *Energy Environ Sci.* 2018;11(10):2876-2883.

21. Tang X, Wang P, Bai M, et al. Unveiling the reversibility and stability origin of the aqueous V_2O_5-Zn batteries with a $ZnCl_2$ "water-in-salt" electrolyte. *Adv Sci (Weinh).* 2021;8(23):e2102053.

22. Yang Y, Tang Y, Fang G, et al. Li^+ intercalated $V_2O_5 \cdot nH_2O$ with enlarged layer spacing and fast ion diffusion as an aqueous zinc-ion battery cathode. *Energy Environ Sci.* 2018;11(11):3157-3162.

23. Liu C, Neale Z, Zheng J, et al. Expanded hydrated vanadate for high-performance aqueous zinc-ion batteries. *Energy Environ Sci.* 2019;12(7):2273-2285.

24. Liu S, Zhu H, Zhang B, et al. Tuning the kinetics of zinc-ion insertion/extraction in V_2O_5 by in situ polyaniline intercalation enables improved aqueous zinc-ion storage performance. *Adv Mater.* 2020;32(26):e2001113.

25. Fan C-Y, Zheng Y-P, Zhang X-H, et al. High-performance and low-temperature lithium-sulfur batteries: synergism of thermodynamic and kinetic regulation. *Adv Energy Mater.* 2018;8(18):1703638.

26. Zheng X, Gu Z, Fu J, et al. Knocking down the kinetic barriers towards fast-charging and low-temperature sodium metal batteries. *Energy Environ Sci.* 2021;14(9):4936-4947.

27. Chang Z, Yang H, Qiao Y, Zhu X, He P, Zhou H. Tailoring the solvation sheath of cations by constructing electrode front-faces for rechargeable batteries. *Adv Mater.* 2022;34(34):e2201339.

28. Zhang Q, Ma Y, Lu Y, et al. Modulating electrolyte structure for ultralow temperature aqueous zinc batteries. *Nat Commun.* 2020;11(1):4463.

29. Zhao M, Lv Y, Zhao S, et al. Simultaneously stabilizing both electrodes and electrolytes by a self-separating organometallics interface for high-performance zinc-ion batteries at wide temperatures. *Adv Mater.* 2022;34(49):e2206239.

30. Blanc LE, Kundu D, Nazar LF. Scientific challenges for the implementation of Zn-ion batteries. *Joule.* 2020;4(4):771-799.

31. Cui F, Wang D, Hu F, et al. Deficiency and surface engineering boosting electronic and ionic kinetics in $NH_4V_4O_{10}$ for high-performance aqueous zinc-ion battery. *Energy Storage Mater.* 2022;44:197-205.

32. Kundu D, Hosseini Vajargah S, Wan L, Adams B, Prendergast D, Nazar LF. Aqueous vs. nonaqueous Zn-ion batteries: consequences of the desolvation penalty at the interface. *Energy Environ Sci.* 2018;11(4):881-892.

33. Zhao M, Rong J, Huo F, et al. Semi-immobilized ionic liquid regulator with fast kinetics toward highly stable zinc anode under −35 to 60 degrees C. *Adv Mater.* 2022;34(32):e2203153.

34. Xi Y, Ye X, Duan S, et al. Iron vacancies and surface modulation of iron disulfide nanoflowers as a high power/energy density cathode for ultralong-life stable Li storage. *J Mater Chem A.* 2020;8(29):14769-14777.

35. Guo C, Yi S, Si R, et al. Advances on defect engineering of vanadium-based compounds for high-energy aqueous zinc–ion batteries. *Adv Energy Mater.* 2022;12(40):2202039.

36. Zhang J, You C, Lin H, Wang J. Electrochemical kinetics modulators in lithium sulfur batteries: from defect-rich catalysts to single atomic catalysts. *Energy Environ Mater.* 2021;5(3):731-750.

37. Liu F, Yu Q, Xue J, et al. Bimetallic alloys b-As_xP_{1-x} at high concentration differences: ideal for photonic devices. *J Phys Chem Lett.* 2022;13(40):9501-9509.

38. Zhang Y, Cao Z, Liu S, et al. Charge-enriched strategy based on MXene-based polypyrrole layers toward dendrite-free zinc metal anodes. *Adv Energy Mater.* 2022;12(13):2103979.

39. He T, Weng S, Ye Y, et al. Cation-deficient $Zn_{0.3}(NH_4)_{0.3}V_4O_{10} \cdot 0.91H_2O$ for rechargeable aqueous zinc battery with superior low-temperature performance. *Energy Storage Mater.* 2021;38:389-396.

40. Xiong T, Yu ZG, Wu H, et al. Defect engineering of oxygen-deficient manganese oxide to achieve high-performing aqueous zinc ion battery. *Adv Energy Mater.* 2019;9(14):1803815.

41. Liao M, Wang J, Ye L, et al. A deep-cycle aqueous zinc-ion battery containing an oxygen-deficient vanadium oxide cathode. *Angew Chem Int Ed Engl.* 2020;59(6):2273-2278.

42. Zhang Y, Tao L, Xie C, et al. Defect engineering on electrode materials for rechargeable batteries. *Adv Mater.* 2020;32(7):e1905923.

43. Kondo Y, Abe T, Yamada Y. Kinetics of interfacial ion transfer in lithium-ion batteries: mechanism understanding and improvement strategies. *ACS Appl Mater Interfaces.* 2022;14(20):22706-22718.

44. Wang J, Jia L, Zhong J, et al. Single-atom catalyst boosts electrochemical conversion reactions in batteries. *Energy Storage Mater.* 2019;18:246-252.

45. Wang J, Jia L, Liu H, et al. Multi-ion modulated single-step synthesis of a nanocarbon embedded with a defect-rich nanoparticle catalyst for a high loading sulfur cathode. *ACS Appl Mater Interfaces.* 2020;12(11):12727-12735.

46. Cheng S, Wang J, Duan S, et al. Anionic oxygen vacancies in Nb_2O_{5-x} carbon hybrid host endow rapid catalytic behaviors for high-performance high areal loading lithium sulfur pouch cell. *Chem Eng J.* 2021;417:128172.

47. Wang J, Zhang J, Cheng S, et al. Long-life dendrite-free lithium metal electrode achieved by constructing a single metal atom anchored in a diffusion modulator layer. *Nano Lett.* 2021;21(7):3245-3253.

48. Zhang J, He R, Zhuang Q, et al. Tuning 4f-center electron structure by Schottky defects for catalyzing Li diffusion to achieve long-term dendrite-free lithium metal battery. *Adv Sci (Weinh).* 2022;9(23):e2202244.

49. Ma Q, Gao R, Liu Y, et al. Regulation of outer solvation shell toward superior low-temperature aqueous zinc-ion batteries. *Adv Mater.* 2022;34(49):e2207344.

50. Wang J, Zhang J, Wu J, et al. Interfacial "single-atom-in-defects" catalysts accelerating Li^+ desolvation kinetics for long-lifespan lithium-metal batteries. *Adv Mater.* 2023;35(39):e2302828.

51. Li L, Tu H, Wang J, et al. Electrocatalytic MOF-carbon bridged network accelerates Li^+-solvents desolvation for high Li^+ diffusion toward rapid sulfur redox kinetics. *Adv Funct Mater.* 2023;33(13):2212499.

52. Zhang X, Li XY, Zhang YZ, et al. Accelerated Li^+ desolvation for diffusion booster enabling low-temperature sulfur redox kinetics via electrocatalytic carbon-grafted-CoP porous nanosheets. *Adv Funct Mater.* 2023;33(36):2302624.

53. Shin J, Choi DS, Lee HJ, Jung Y, Choi JW. Hydrated intercalation for high-performance aqueous zinc ion batteries. *Adv Energy Mater.* 2019;9(14):1900083.

54. Raccichini R, Varzi A, Passerini S, Scrosati B. The role of graphene for electrochemical energy storage. *Nat Mater.* 2015;14(3):271-279.

55. Du M, Miao Z, Li H, et al. Oxygen-vacancy and phosphate coordination triggered strain engineering of vanadium oxide

for high-performance aqueous zinc ion storage. *Nano Energy.* 2021;89:106477.

56. Peng X, Zhang X, Wang L, et al. Hydrogenated V_2O_5 nanosheets for superior lithium storage properties. *Adv Funct Mater.* 2016;26(5):784-791.

57. Liang X, Yan L, Li W, et al. Flexible high-energy and stable rechargeable vanadium-zinc battery based on oxygen defect modulated V_2O_5 cathode. *Nano Energy.* 2021;87:106164.

58. Qi Z, Xiong T, Chen T, et al. Harnessing oxygen vacancy in V_2O_5 as high performing aqueous zinc-ion battery cathode. *J Alloys Comp.* 2021;870:159403.

59. Li X, Guan Q, Zhuang Z, et al. Ordered mesoporous carbon grafted MXene catalytic heterostructure as Li-ion kinetic pump toward high-efficient sulfur/sulfide conversions for Li-S battery. *ACS Nano.* 2023;17(2):1653-1662.

60. He W, Lin Z, Zhao K, et al. Interspace and vacancy modulation: promoting the zinc storage of an alcohol-based organic–inorganic cathode in a water-organic electrolyte. *Adv Mater.* 2022;34(47):e2203920.

61. Liu F, Chen Z, Fang G, et al. V_2O_5 nanospheres with mixed vanadium valences as high electrochemically active aqueous zinc-ion battery cathode. *Nanomicro Lett.* 2019;11(1):25.

62. Zhang Y, Wan F, Huang S, Wang S, Niu Z, Chen J. A chemically self-charging aqueous zinc-ion battery. *Nat Commun.* 2020;11(1):2199.

63. Ding S, Zhang M, Qin R, et al. Oxygen-deficient beta-MnO_2@graphene oxide cathode for high-rate and long-life aqueous zinc ion batteries. *Nanomicro Lett.* 2021;13(1):173.

64. Luo H, Wang B, Wu F, et al. Synergistic nanostructure and heterointerface design propelled ultra-efficient in-situ self-transformation of zinc-ion battery cathodes with favorable kinetics. *Nano Energy.* 2021;81:105601.

65. Zhou J, Dong A, Du L, et al. Mn-doped ZnO microspheres as cathode materials for aqueous zinc ion batteries with ultrastability up to 10000 cycles at a large current density. *Chem Eng J.* 2021;421:127770.

66. Chen H, Huang J, Tian S, et al. Interlayer modification of pseudocapacitive vanadium oxide and $Zn(H_2O)_n^{2+}$ migration regulation for ultrahigh rate and durable aqueous zinc-ion batteries. *Adv Sci (Weinh).* 2021;8(14):e2004924.

67. Liu Y, Dai Z, Zhang W, et al. Sulfonic-group-grafted $Ti_3C_2T_x$ MXene: a silver bullet to settle the instability of polyaniline toward high-performance Zn-ion batteries. *ACS Nano.* 2021;15(5):9065-9075.

68. Guan X, Sun Q, Sun C, et al. Tremella-like hydrated vanadium oxide cathode with an architectural design strategy toward ultralong lifespan aqueous zinc-ion batteries. *ACS Appl Mater Interfaces.* 2021;13(35):41688-41697.

69. Wu S, Liu S, Hu L, Chen S. Constructing electron pathways by graphene oxide for V_2O_5 nanoparticles in ultrahigh-performance and fast charging aqueous zinc ion batteries. *J Alloys Comp.* 2021;878:160324.

70. Ma X, Cao X, Yao M, et al. Organic–inorganic hybrid cathode with dual energy-storage mechanism for ultrahigh-rate and ultralong-life aqueous zinc-ion batteries. *Adv Mater.* 2022;34(6):e2105452.

71. Liang P, Xu T, Zhu K, et al. Heterogeneous interface-boosted zinc storage of $H_2V_3O_8$ nanowire/$Ti_3C_2T_x$ MXene composite toward high-rate and long cycle lifespan aqueous zinc-ion batteries. *Energy Storage Mater.* 2022;50:63-74.

72. Zhao Y, Zhang P, Liang J, et al. Uncovering sulfur doping effect in MnO_2 nanosheets as an efficient cathode for aqueous zinc ion battery. *Energy Storage Mater.* 2022;47:424-433.

73. Liang W, Rao D, Chen T, Tang R, Li J, Jin H. $Zn_{0.52}V_2O_{5-a}\cdot 1.8H_2O$ cathode stabilized by in situ phase transformation for aqueous zinc-ion batteries with ultra-long cyclability. *Angew Chem Int ed Engl.* 2022;61(35): e202207779.

74. Gao S, Ju P, Liu Z, et al. Electrochemically induced phase transition in a nanoflower vanadium tetrasulfide cathode for high-performance zinc-ion batteries. *J Energy Chem.* 2022;69: 356-362.

75. Bi W, Gao G, Wu G, Atif M, AlSalhi MS, Cao G. Sodium vanadate/PEDOT nanocables rich with oxygen vacancies for high energy conversion efficiency zinc ion batteries. *Energy Storage Mater.* 2021;40:209-218.

76. Yang X, Rogach AL. Electrochemical techniques in battery research: a tutorial for nonelectrochemists. *Adv Energy Mater.* 2019;9(25):1900747.

77. Zhang F, Du M, Miao Z, et al. Oxygen vacancies and N-doping in organic–inorganic pre-intercalated vanadium oxide for high-performance aqueous zinc-ion batteries. *InfoMat.* 2022;4(11): e12346.

78. Cao J, Zhang D, Yue Y, et al. Revealing the impacts of oxygen defects on Zn^{2+} storage performance in V_2O_5. *Mater Today Energy.* 2021;21:100824.

79. He T, Ye Y, Li H, et al. Oxygen-deficient ammonium vanadate for flexible aqueous zinc batteries with high energy density and rate capability at $-30°C$. *Mater Today.* 2021;43:53-61.

80. Zhao Q, Song A, Ding S, et al. Preintercalation strategy in manganese oxides for electrochemical energy storage: review and prospects. *Adv Mater.* 2020;32(50):e2002450.

81. Wang J, Hu H, Duan S, et al. Construction of moisture-stable lithium diffusion-controlling layer toward high performance dendrite-free lithium anode. *Adv Funct Mater.* 2022;32(12): 2110468.

82. Montenegro A, Dutta C, Mammetkuliev M, et al. Asymmetric response of interfacial water to applied electric fields. *Nature.* 2021;594(7861):62-65.

83. Li E, Liu C, Lin H, et al. Bonding strength regulates anchoring-based self-assembly monolayers for efficient and stable perovskite solar cells. *Adv Funct Mater.* 2021;31(35):2103847.

84. Zhang H, Guo G, Adenusi H, et al. Advances and issues in developing intercalation graphite cathodes for aqueous batteries. *Mater Today.* 2022;53:162-172.

SUPPORTING INFORMATION

Additional supporting information can be found online in the Supporting Information section at the end of this article.